

Source characterization and modeling development for monoenergetic-proton radiography experiments on OMEGA

M. J.-E. Manuel, A. B. Zylstra, H. G. Rinderknecht, D. T. Casey, M. J. Rosenberg et al.

Citation: *Rev. Sci. Instrum.* **83**, 063506 (2012); doi: 10.1063/1.4730336

View online: <http://dx.doi.org/10.1063/1.4730336>

View Table of Contents: <http://rsi.aip.org/resource/1/RSINAK/v83/i6>

Published by the [American Institute of Physics](#).

Related Articles

Spatiotemporal correlation between microdischarges in concentric ring pattern in dielectric barrier discharge at atmospheric pressure

Phys. Plasmas **19**, 062308 (2012)

Lasing of extreme ultraviolet light with nitrogen plasma in a recombining phase—Roles of doubly excited states

Phys. Plasmas **19**, 063302 (2012)

Parallel transport of long mean-free-path plasma along open magnetic field lines: Parallel heat flux

Phys. Plasmas **19**, 062501 (2012)

Plasma ion source for in situ ion bombardment in a soft x-ray magnetic scattering diffractometer

Rev. Sci. Instrum. **83**, 053303 (2012)

Generation of tunable, 100–800 MeV quasi-monoenergetic electron beams from a laser-wakefield accelerator in the blowout regime

Phys. Plasmas **19**, 056703 (2012)

Additional information on *Rev. Sci. Instrum.*

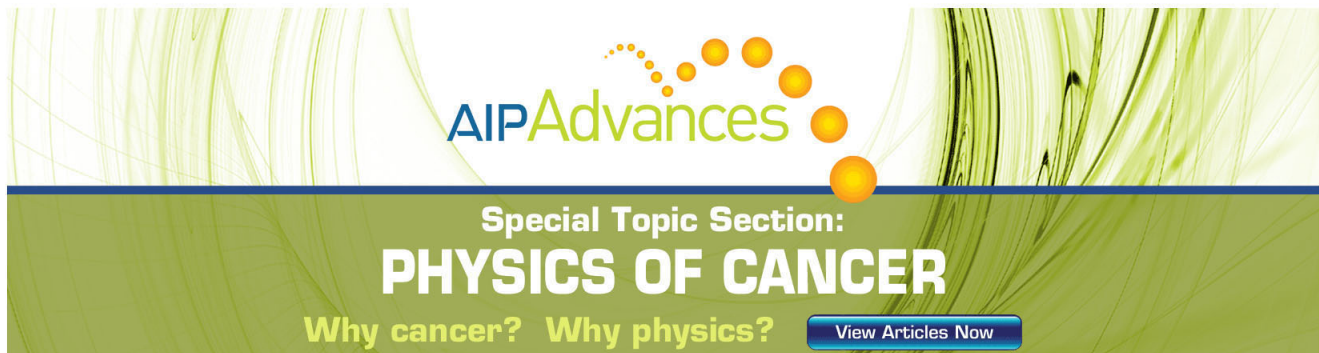
Journal Homepage: <http://rsi.aip.org>

Journal Information: http://rsi.aip.org/about/about_the_journal

Top downloads: http://rsi.aip.org/features/most_downloaded

Information for Authors: <http://rsi.aip.org/authors>

ADVERTISEMENT



AIP Advances

Special Topic Section:
PHYSICS OF CANCER

Why cancer? Why physics? [View Articles Now](#)

Source characterization and modeling development for monoenergetic-proton radiography experiments on OMEGA

M. J.-E. Manuel, A. B. Zylstra, H. G. Rinderknecht, D. T. Casey, M. J. Rosenberg, N. Sinenian, C. K. Li, J. A. Frenje, F. H. Séguin, and R. D. Petrasso
Plasma Science and Fusion Center, Massachusetts Institute of Technology, 77 Massachusetts Avenue, Cambridge, Massachusetts 02139, USA

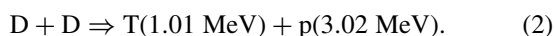
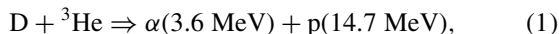
(Received 23 April 2012; accepted 4 June 2012; published online 22 June 2012)

A monoenergetic proton source has been characterized and a modeling tool developed for proton radiography experiments at the OMEGA [T. R. Boehly *et al.*, *Opt. Comm.* **133**, 495 (1997)] laser facility. Multiple diagnostics were fielded to measure global isotropy levels in proton fluence and images of the proton source itself provided information on local uniformity relevant to proton radiography experiments. Global fluence uniformity was assessed by multiple yield diagnostics and deviations were calculated to be $\sim 16\%$ and $\sim 26\%$ of the mean for DD and $D^3\text{He}$ fusion protons, respectively. From individual fluence images, it was found that the angular frequencies of $\gtrsim 50 \text{ rad}^{-1}$ contributed less than a few percent to local nonuniformity levels. A model was constructed using the Geant4 [S. Agostinelli *et al.*, *Nuc. Inst. Meth. A* **506**, 250 (2003)] framework to simulate proton radiography experiments. The simulation implements realistic source parameters and various target geometries. The model was benchmarked with the radiographs of cold-matter targets to within experimental accuracy. To validate the use of this code, the cold-matter approximation for the scattering of fusion protons in plasma is discussed using a typical laser-foil experiment as an example case. It is shown that an analytic cold-matter approximation is accurate to within $\lesssim 10\%$ of the analytic plasma model in the example scenario. © 2012 American Institute of Physics. [<http://dx.doi.org/10.1063/1.4730336>]

I. INTRODUCTION

Monoenergetic proton radiography has been used to infer path-integrated electric and magnetic field strengths in many high energy density physics experiments.¹⁻⁵ This unique diagnostic technique provides a method to experimentally probe plasmas for electric and magnetic fields in regimes where other traditional methods (Langmuir probes, B-dot probes, Faraday rotation, etc.) do not work or are impractical. Imaging protons are deflected by electromagnetic fields in the plasma through the Lorentz force, but do not otherwise perturb the overall plasma evolution. In this way, path-integrated field strength information becomes encoded within modulations observed in proton fluence images. Therefore, it is important to understand the local fluence uniformity characteristics of the backlighter source to be able to accurately deduce quantitative information about the plasma subject.

Fusion protons are generated through irradiation of an “exploding-pusher” shock-driven capsule. This unique backlighting source emits monoenergetic protons quasi-isotropically, providing the ability to perform multiple experiments on a single shot. Capsules are filled with $D^3\text{He}$ gas to produce the following fusion reactions:



Furthermore, because the backlighter source is monoenergetic ($\Delta E/E \sim 3\%$) in nature, there is a one-to-one mapping of deflection angle to path-integrated field strength. Radiographs are recorded on CR-39 nuclear track detectors⁶⁻⁹ where

absolute location and track characteristics are stored for incident charged particles. Typically, two pieces of CR-39 are fielded, each one filtered to register either DD or $D^3\text{He}$ protons whereby individual images of absolute proton fluence are easily generated for each species.

This technique is in strong contrast to a complementary method of generating $\sim \text{MeV}$ protons for radiography using a short-pulse, high-intensity laser, and the Target Normal Sheath Acceleration (TNSA) mechanism.¹⁰⁻¹² Both methods provide high energy protons useful for probing high energy density plasmas. The TNSA method provides higher spatial and temporal resolution than the exploding-pusher capsule. Images are typically recorded on a filtered stack of radiochromic film, where each film has a dominant proton energy window to which it is sensitive.¹² However, there can be a degeneracy in energy between the source continuum and energy loss in dense plasmas, depending on the configuration and field structure under observation, due to the exponential proton distribution.¹³ Contrarily, the exploding-pusher backlighter generates an isotropic monoenergetic proton source. In conjunction with a filter-matched detector array that counts individual proton tracks, the complete diagnostic system provides a unique approach to accurately measuring electric and magnetic fields that were otherwise unmeasurable.

While protons are sensitive to field structures in the plasma, they also interact with ions and electrons through Coulomb collisions. Energy loss and scattering due to Coulomb interactions are inherently statistical processes and may be accounted for using a Monte Carlo¹⁴ approach. A simulation has been constructed using the Geant4 (Refs. 15 and 16) framework to accurately model these effects on the

spatial and spectral resolution of proton radiographs. Because Geant4 is open-source code, proton trajectories may be tracked through arbitrarily defined three-dimensional electromagnetic field geometries and mass distributions. Together with a thorough understanding of the backlighter source, this modeling tool provides the capabilities to simulate many proton radiography experiments and generate synthetic radiographs for direct comparison with experimental data.

This paper is organized as follows. Section II provides an overview of the OMEGA laser system and its capabilities. The experimental methodology used to determine backlighter isotropy is discussed in Sec. III along with a brief overview of experiments performed to benchmark proton radiography simulations. Section IV describes the monoenergetic proton source and its characteristics with a detailed discussion on proton fluence isotropy. Modeling of the proton radiographic system using the Geant4 toolkit is presented in Sec. V along with a validation of the cold matter approximation and benchmark experiments. This paper concludes with a summary of the results from this work in Sec. VI.

II. OMEGA LASER SYSTEM

The OMEGA laser¹⁷ system provides a unique ability to study fusion with fusion. It is composed of 60 individual beams that are frequency tripled upon entrance to the vacuum chamber to a wavelength of $\lambda \sim 0.351 \mu\text{m}$. Each laser beam has a nominal maximum energy of 500 J (for a total of 30 kJ in all beams), which can be pointed to any location within 1 cm of target chamber center. Beams enter the spherical target chamber in a truncated icosahedron (“soccer ball”) pattern and may be split into three different “legs” of 20 beams each. Two separate drivers can be used to allow two different pulse shapes with independent timings to drive individual targets. An Aitoff projection of the target chamber layout is shown in Figure 1 for the orientation of beam legs and diagnostic ports. A typical beam configuration is illustrated where Legs 1 and 3 may be used to drive a target using different types of pulse shapes at various intensities and Leg 2 is used to drive the

fusion-proton backlighter. Independent laser drives and the range of pointing capabilities on OMEGA provide the unique ability to create a plasma with one set of beams and drive a monoenergetic proton backlighter to radiograph the plasma with another.

III. EXPERIMENTAL METHODS

Experiments were performed to examine proton backlighter isotropy by fielding multiple proton yield diagnostics. The OMEGA port map shown in Figure 1 indicates backlighter isotropy diagnostics (green). Four diagnostics measured D^3He -proton yield and three measured DD-proton yield, providing data on the global isotropy of both proton species. Diagnostic ports TIM2 and TIM3 were configured to radiograph the backlighter source itself to study local uniformity on a scale specifically relevant to proton radiography.

Validation experiments were also performed to benchmark Geant4 simulations of scattering in cold matter. In these experiments, non-irradiated subjects were radiographed so that the mass distributions were well known. The first benchmark discussed in Sec. V B is a CH capsule where protons sampled various areal densities throughout the shell. Both DD and D^3He proton radiographs were taken and fluence images were compared to synthetic data. The second benchmark was concerned with scattering at various frequencies in different thicknesses of CH. In these experiments, D^3He proton fluence radiographs were analyzed using a Fourier analysis technique to compare synthetic and experimental data.

In all diagnostics, backlighter protons were incident on 1.5-mm thick sheets of CR-39, a plastic nuclear track detector.⁶ After proton exposure, pieces were etched in a 6N NaOH solution for 1–6 h, depending on fluence level, to reveal tracks created by charged particles. Etched CR-39 samples were scanned using an automated optical microscope system whereby track locations, diameters, eccentricities, and contrast levels (relative to the background) are recorded and stored for later analysis. Using detailed track information, proton fluence images were generated, and

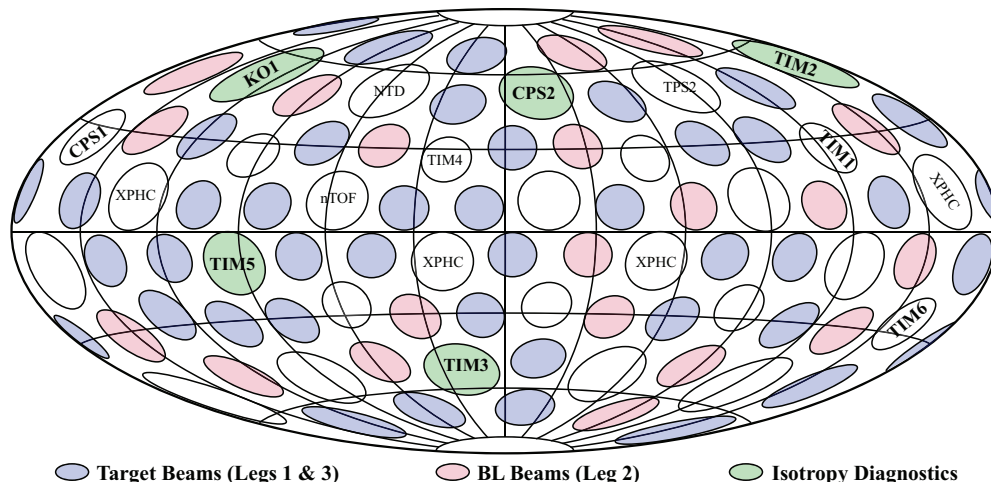


FIG. 1. An Aitoff projection of the OMEGA target chamber. The 60 beams are split into three legs. In typical experiments, Legs 1 and 3 (blue) are used to drive a target and Leg 2 (red) drives the proton backlighter source. Ports used to field proton fluence diagnostics are also shown (green) and labeled. Other diagnostic ports not used are labeled for reference.

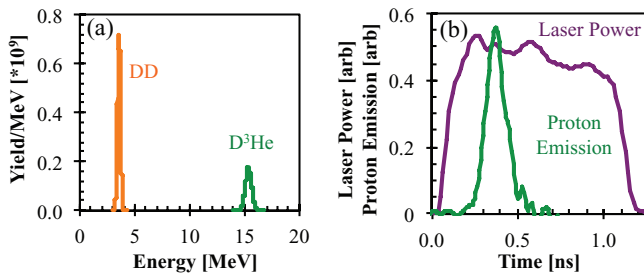


FIG. 2. (a) Sample fusion proton spectra from an exploding pusher backlighter capsule taken from OMEGA shot 51237. DD protons were measured at 3.6 MeV with FWHM of 320 keV and D^3He protons were measured at 15.3 MeV with FWHM of 670 keV. (b) Sample emission profile for D^3He protons overlaid on the 1 ns square pulse used to drive the capsule on OMEGA shot 51237. Bang time was measured at 420 ps after laser onset with FWHM of 140 ps.

because of the known relationship between particle energy and track diameter,^{7,8} an image of relative proton energy may also be produced.

IV. CHARACTERIZATION OF A MONOENERGETIC-PROTON SOURCE

A. Fusion-proton production

Exploding-pushers have been used to generate fusion-protons for backlighting in many experiments^{1,3-5} at the OMEGA laser facility. Capsules are nominally 420 μm in diameter with a 2.0 μm -thick glass shell and filled with equimolar D^3He gas (6 atm D_2 , 12 atm 3He) to produce fusion protons. Characteristic spectra of DD and D^3He protons emitted from backlighter capsules are shown in Figure 2(a). In typical configurations, backlighter capsules are irradiated with 20 OMEGA beams¹⁸ without smoothing by spectral dispersion or distributed phase plates for a total of ~ 9 kJ on target in a 1 ns square pulse as shown in Figure 2(b). Fusion proton spectra are broadened ($\sim 9\%$ and $\sim 4\%$ FWHM for DD and D^3He , respectively) by thermal effects and by time-varying E fields around the implosion capsule when nuclear production occurs during the laser pulse.^{6,19} The E fields are caused by a net positive charge on the capsule during laser irradiation and this charging effect produces an energy upshift of ~ 300 – 600 keV in fusion protons. In exploding pushers of the specified dimensions, nuclear production always takes place during the 1 ns drive.

The proton temporal diagnostic (PTD)²⁰ was used to measure peak fusion production (bang time) for D^3He protons. Previous experiments using 17, 20, or 30 beams on the backlighter, but still filled with 18 atm of D^3He , were examined. It was found that measured bang times fit a normal distribution well with a mean of 486 ± 5 ps after laser onset and a standard deviation of 35 ± 4 ps. When the on-target energy was increased by a factor of ~ 2 , no systematic change in bang time was observed. This result indicates that increasing on-target energy above ~ 7700 J does not appreciably increase the shock transit time in these exploding pusher capsules.

Timing of the proton source with respect to other laser beams is essential for radiography experiments. Without dedicating extra experiments to tuning timing fiducials, PTD has

an absolute uncertainty of ± 50 ps, dominating the timing error. However, based on many experiments, 95% of proton backlighters will have a bang time of 486 ± 70 ps; though it should still be measured by PTD for each shot when possible. Also, the typical burn duration for these types of capsules was found to have a FWHM of ~ 150 ps, which sets the temporal resolution of the radiography system. The fusion burn region has an approximately Gaussian radial profile with a FWHM of ~ 45 μm (Ref. 1) that emits protons in a quasi-isotropic fashion. DD and D^3He proton data have been obtained to quantify the isotropy of this backlighting technique.

B. Proton emission isotropy

Multiple diagnostics were fielded as indicated in Figure 1 to measure large and small scale proton fluence uniformity. The charged-particle spectrometer (CPS2) (Ref. 21 and 22) momentum analyzed charged particles passing through an aperture and energy spectra were recorded on CR-39 detectors. A filtered stack of 10 cm \times 10 cm sheets of CR-39 was fielded in TIM2 to image the backlighter's DD and D^3He protons. TIM3 held a single 7 cm round sheet of CR-39 that was filtered for DD protons only. To measure proton bang time and D^3He yield, PTD was fielded in TIM5. Lastly, an aluminum wedge range filter (WRF) (Ref. 6) in KO1 measured the time-integrated D^3He -proton energy spectrum. Radiographs of the backlighter in TIM2 (squares) and TIM3 (circles) provided short scale-length information on single sheets of CR-39, whereas long scale-length fluctuations were measured using the port-to-port variation in the inferred yield.

These diagnostics provided four measurements of D^3He protons and three measurements of DD protons at different port locations. The results of multiple experiments to investigate backlighter isotropy are shown in Figure 3. Measurements of DD and D^3He yields into 4π are shown for multiple angles in Figures 3(a) and 3(b). Each yield measurement is represented by a different symbol and the statistical mean is denoted by (\times). Error bars in these plots are calculated as the standard deviation (variance) of the yield measurements and are plotted against the average DD and D^3He yields in Figures 3(c) and 3(d). A slight increase in global variance with average yield may be inferred from these data, but this is inconclusive within the scatter. The global variance for DD and D^3He protons can be accurately characterized by a simple mean and deviation as $\Sigma_{DD} \approx 16 \pm 7\%$ and $\Sigma_{D^3He} \approx 26 \pm 10\%$, respectively. The measured global variance for D^3He protons in these 20 beam exploding-pusher capsules is slightly higher than those quoted by Séguin *et al.*²³ for 60 beam implosions of 20 μm thick CH shells. However, capsules in those experiments were thicker and larger than the exploding-pushers such that peak fusion production occurred > 500 ps after the laser pulse.

Local variation in proton fluence was assessed through “blank” radiographs, shown in Figures 3(g) and 3(h). CR-39 sheets were fielded in TIM2 and TIM3 to image the backlighter without a subject in the field of view. These images provided proton fluence distributions over different solid angles. The 10 cm square CR-39 fielded in TIM2 was placed

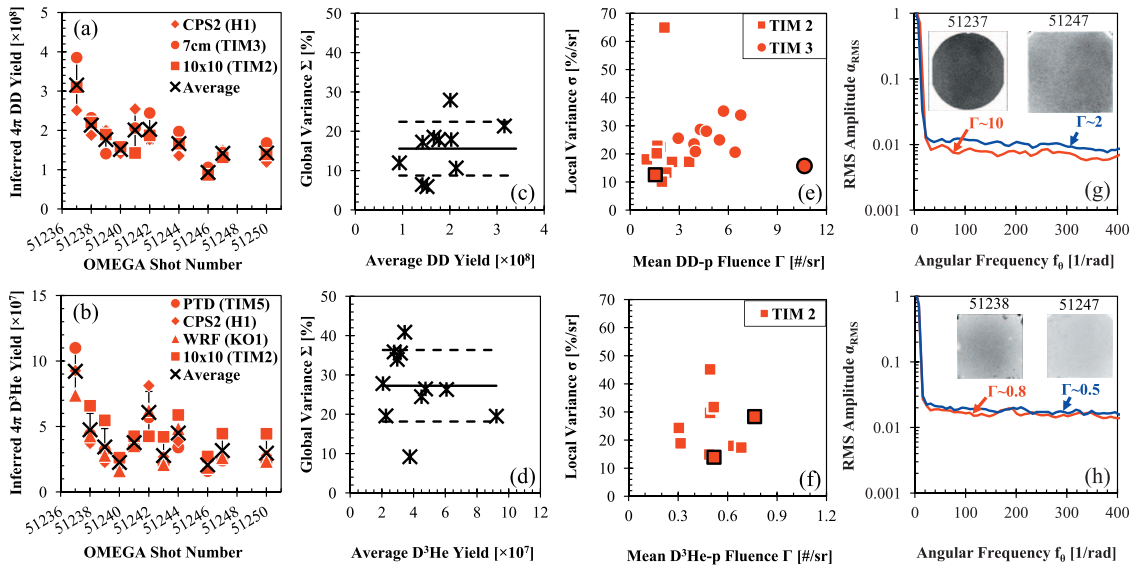


FIG. 3. Summary of backlighter proton emission isotropy data. (a) and (b) DD and $D^3\text{He}$ -proton yield measurements from different ports; error bars are calculated standard deviations. (c) and (d) Global (long-scale) variance of yield measurements as a function of mean yield. Average variance Σ is shown by the solid line and the dashed lines are \pm one standard deviation. (e) and (f) Local proton variance σ measured from radiographs in TIM2 (10 cm squares) and TIM3 (7 cm circles) as a function of mean proton fluence Γ . (g) and (h) Average power density spectrum plotted as a function of angular frequency for two points in each of (e) and (f) (outlined in black) with corresponding radiographs where darker pixels indicate higher fluence. Frequencies $\gtrsim 50 \text{ rad}^{-1}$ are shown to have amplitudes of $\leq 3\%$ relative to the mean proton fluence level (normalized to 1). These data indicate that most of the local variance stems from long-scale perturbations.

27.18 cm from the backlighter covering $\sim 0.13 \text{ sr}$ and 7 cm round CR-39 fielded in TIM3 were 21.88 cm away covering $\sim 0.08 \text{ sr}$. Because detectors are fielded at different distances, and fluence fluctuations due to the backlighter itself are of particular interest, numerical statistics are removed from local fluence variation σ by:

$$\sigma = \frac{\sqrt{\sigma_{\Gamma-\text{meas}}^2 - \sigma_{\Gamma-\text{stat}}^2}}{\langle \Gamma_{\text{meas}} \rangle}, \quad (3)$$

where $\sigma_{\Gamma-\text{meas}}$ is the measured statistical deviation of protons per steradian, $\langle \Gamma_{\text{meas}} \rangle$ is the statistical mean proton fluence used to normalize the variation across different experiments, and $\sigma_{\Gamma-\text{stat}}$ is the numeric statistical variation per steradian $\sim \sqrt{\langle \Gamma_{\text{meas}} \rangle}$. Figures 3(e) and 3(f) show the results of statistically corrected local variance measurements as a function of mean fluence over multiple experiments. The variance in DD-proton fluence was observed to increase slightly with the mean as shown in Figure 3(e) despite the two outliers. However, no trend is observed within the scatter of a single detector (in TIM2 or TIM3), this trend is only significant when combining the results from TIM2 and TIM3. This could be simply explained by a higher local variance in the TIM3 direction than in the TIM2 direction; no trend is observed in $D^3\text{He}$ measurements from TIM2 within the scatter. As in the case for global variance, the local variance of $D^3\text{He}$ protons ($\sigma_{D^3\text{He}}$) is measured to be slightly higher than that of the DD protons (σ_{DD}). The absolute magnitude of the standard deviations for $D^3\text{He}$ proton fluence are smaller than those of DD protons, but due to lower average fluences, the relative percent-variations for $D^3\text{He}$ protons are measured higher. Proton fluence fluctuations in “blank” radiographs were characterized using a discrete Fourier transform (DFT) technique.

Sample proton radiographs and corresponding average mode spectra are shown in Figures 3(g) and 3(h). Lineouts of proton fluence were taken at multiple angles and processed using a one dimensional DFT technique with a Hann windowing function to reduce power leakage.²⁴ The absolute sinusoidal amplitude α_{abs} corresponding to a power density P_f at a given nonzero frequency is $\alpha_{\text{abs}} \propto \sqrt{2P_f}$, where the proportionality constant is dependent on the normalization of the power spectra. However, the important metric here is the perturbation amplitude relative to the average (zero frequency) fluence $\alpha_0 \propto \sqrt{P_0}$. The normalized amplitude is defined as $\alpha = \sqrt{2P_f/P_0}$. Furthermore, because α is the amplitude of a sinusoid, the normalized RMS amplitude at a given nonzero frequency is simply $\alpha_{\text{RMS}} = \sqrt{P_f/P_0}$. Because spherical symmetry is assumed, DFTs over all angles are averaged to obtain an overall sense of mode structure in proton fluence.

Spatial frequencies in the detector plane were converted to angular frequencies ($f_\theta = 1/\theta$) for the comparison of mode structure measurements at different distances from the backlighter; results are shown in Figures 3(g) and 3(h). These amplitude spectra are not corrected for statistics, and it is clear that more proton fluence reduces the relative amplitude of high mode perturbations, as expected. The sample spectra shown clearly indicate that low mode perturbations dominate the local variance observed in Figures 3(e) and 3(f). RMS amplitudes calculated for angular frequencies $\gtrsim 50 \text{ rad}^{-1}$ are less than a few percent relative to the average proton fluence. These data indicate that when taking lineouts through proton fluence radiographs, local nonuniformities due to the backlighter are quite small for angles less than ~ 0.02 radians ($\sim 1.1^\circ$). Local and global variance of fusion protons discussed here is larger than other similar measurements,²³

but much of this variation may be attributed to lower illumination uniformity and bang time occurring during the laser pulse. Long scale-length variation $\gtrsim 50\%$ across a single CR-39 sample may be expected and must be considered when quantitatively analyzing proton fluence over large solid angles and when comparing to synthetic data.

V. MODELING USING GEANT4

To model proton radiography experiments, a Monte Carlo code was written using the Geant4 toolkit.^{15,16} The *geometry and tracking* code is an open source library of functions written in C++. The experimental system was constructed within the Geant4 framework (version 4.9.4.p01) through proper geometry, material, and physics package²⁵ implementation. To this end, a simulation has been developed employing a spatially finite Gaussian proton source for DD and D³He protons of finite spectral width to create synthetic proton radiographs of various subject types.

Accurate modeling is necessary for quantitative interpretation of proton fluence modulations in some radiography experiments. Tracking of protons through electromagnetic fields is performed in Geant4 using a Cash-Karp algorithm (step size set to ≤ 1 nm). Because Geant4 is open source, the user may define an electromagnetic field of arbitrary complexity and choose from a number of different solvers for the equations of motion. Currently, the simulation implements simple fields due to spherical shells of charge, cylindrical shells of charge or current, or sinusoidal E or B fields of varying spatial dimension. Modeling of the Lorentz force is relatively straight forward; its effect does not change whether particles are traversing a plasma of spatially varying parameters, or standard cold matter. However, the interaction of protons with matter is a collisional process and dependent on the local properties of the material at any given point.

A. The cold matter approximation

Coulomb collision physics models currently implemented in Geant4 do not account for plasma environments, and assume “cold matter” (CM) conditions in solids or gases. The user may define a material of arbitrary atomic composition and density, but separate ion and electron distributions may not be defined. Nonetheless, Coulomb collisions involving high energy ions ($\gtrsim \text{MeV}$) are standard binary Rutherford interactions²⁶ between two charged particles and the caveats of the state of matter may be addressed after a basic review of the two body problem.

In the center-of-mass (CoM) reference frame, the angular differential cross section for this Rutherford scattering process is given by²⁶

$$\frac{d\sigma}{d\Omega} = \frac{b_{90}^2}{4} \frac{1}{\sin^4(\theta/2)}, \quad (4)$$

where θ is the exit angle of the particles after the collision in the CoM. The so-called 90° impact parameter²⁷ b_{90} is depen-

TABLE I. Integration limits for the mean square scattering angle $\langle \theta^2 \rangle$ calculation under cold-matter and plasma conditions.

	θ_{min}	θ_{max}
Cold matter	$\max\left(\frac{Z_1 Z_f e_0^2}{2\pi \epsilon_0 m_\mu v_{rel}^2 a}, \frac{\hbar}{m_\mu v_{rel} a}\right)$	$\frac{\hbar}{m_\mu v_{rel} R}$
Plasma	$\max\left(\frac{Z_1 Z_f e_0^2}{2\pi \epsilon_0 m_\mu v_{rel}^2 \lambda_D}, \frac{\hbar}{m_\mu v_{rel} \lambda_D}\right)$	$\frac{\hbar}{m_\mu v_{rel} R}$

dent upon the interacting particle properties by

$$b_{90} = \frac{Z_1 Z_2 e_0^2}{4\pi \epsilon_0} \frac{1}{m_\mu v_{rel}^2}, \quad (5)$$

where Z_1 and Z_2 are the charges of the interacting particles, m_μ is the reduced mass of the system, and v_{rel} is the relative speed between the particles. Coulomb collisions are clearly dominated by small angle scattering due to the $\sim 1/\theta^4$ proportionality in Eq. (4) and diverges as $\theta \rightarrow 0$. To contend with this singularity, physical limits are put on the exit angle (θ_{min} to θ_{max}) when integrating, such that the total cross section is expressed as $\sigma_C \approx \pi b_{90}^2 / \theta_{min}^2$. The upper bound θ_{max} has been neglected here because the cross section is proportional to $\sim 1/\theta^2$. The expression for θ_{min} represents the largest impact parameter (smallest deflection angle) relevant to the situation and is set as the maximum of the classical or quantum limits as described by Jackson²⁶ (see Table I).

In the case where a test particle is incident onto many field particles, as in proton radiography, many successive small angle collisions will occur. Scattering of test protons is caused by momentum exchange with the field particles, therefore similar mass particles (field ions not electrons) will dominate this process. The test proton travels a distance L through the field particles and the probability distribution of exit angles approximates a Gaussian with a mean square scattering angle of²⁶

$$\langle \theta^2 \rangle \simeq 2\pi b_{90}^2 n L \ln \Lambda, \quad (6)$$

where $\Lambda \equiv \theta_{max}/\theta_{min}$ is the argument of the Coulomb logarithm. The result in Eq. (6) was formulated for two interacting charged particles irrespective of the material. However, a simple change of the integration limits is sufficient to estimate the variation of mean scattering angle between plasma and CM.²⁸

Table I provides θ integration limits for both CM and plasma conditions. The maximum scattering angle θ_{max} is set by the quantum limit for the smallest impact parameter R , the nuclear radius, and is approximated²⁶ as $R \approx 1.4 A_f^{1/3}$ fm, where A_f is the mass number of the field particle. The maximum scattering angle limit does not change when looking at interactions in a plasma. However, the minimum scattering angle limit θ_{min} represents the maximum impact parameter in the classical or quantum limit and the shielding scale length will change from CM to a plasma. In CM, this shielding distance is set to the atomic radius a and can be approximated²⁶ as $a \approx 1.4 a_0 Z_f^{-1/3}$, where a_0 is the classical Bohr radius. In a plasma, electric shielding is set by the local Debye length

$$\lambda_D = \sqrt{\frac{\epsilon_0 k_B T_e}{e_0^2 n_e}}, \quad (7)$$

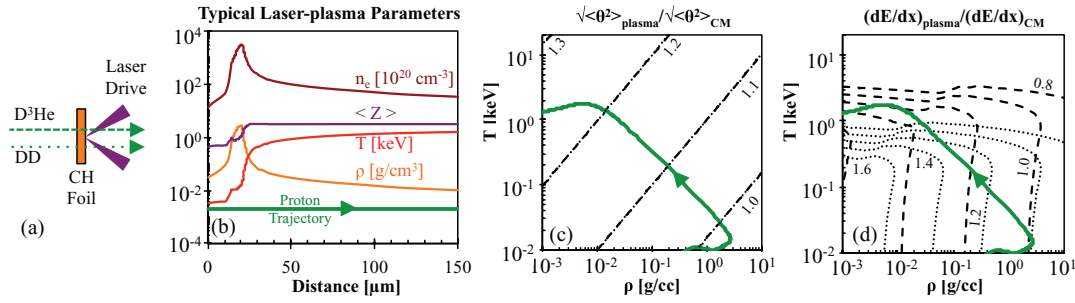


FIG. 4. (a) Schematic of sample laser interaction with a CH foil of initial density 1.04 g/cc. (b) Plasma parameters predicted by DRACO for the sample interaction in (a). The solid (green) line in each plot represents a path through this sample plasma. Contour plots of quantities relevant to Coulomb collisions for 3 MeV (dotted) and 15 MeV (dashed) protons in the temperature-density parameter space of a CH (1:1.38) plasma. (d) The ratio of mean square scattering angle $\sqrt{\langle \theta^2 \rangle}$ in a plasma to that in cold matter. The difference between 3 and 15 MeV protons is negligible, because the ratio is dependent only on $\ln \Lambda$. (d) The ratio of stopping power $\frac{dE}{dx}$ in a plasma to that in cold matter.

where k_B is Boltzmann's constant, T_e is the local electron temperature, and n_e the local electron number density. When calculating the ratio of plasma scattering to CM scattering for a specified plasma, the only remaining term is the Coulomb logarithm.

A trajectory through a sample laser-foil interaction is shown in Figures 4(a) and 4(b). As a test case, these plasma conditions are used to contrast the CM approximation for stopping power and scattering. The plasma parameters were calculated using the DRACO radiation-hydrodynamic code^{29,30} to simulate a 0.351 μm laser of intensity $\sim 4 \times 10^{14} \text{ W/cm}^2$ incident onto a 21 μm CH foil. It is important to note that most energy loss and scattering takes place in the high-density, low-temperature domain when looking along this path due to the much higher mean free path in this regime.

Contours of the plasma-to-CM scattering ratio are shown in Figure 4(c) for 3 and 15 MeV protons in T - ρ space. It is shown that at low temperatures and high densities, there is little difference between scattering in plasma and scattering in CM. To estimate the accuracy of the CM approximation, the sample trajectory shown in Figure 4(c) was path-integrated for both plasma and CM scattering cases through T - ρ space,

$$\theta \approx \sqrt{\int d(\theta^2)}. \quad (8)$$

This calculation indicated that the effective CM scattering would be $\sim 5\%$ lower than that of plasma for both 3 and 15 MeV protons along this trajectory. Because the ratio of scattering angles results in a ratio of Coulomb logarithms, the difference between 3 and 15 MeV protons is negligible as illustrated by the overlaid dotted and dashed curves, but this is not the case when looking at stopping power.

The amount of energy-loss caused by Coulomb collisions can depend on the state of the material. The standard model for energy loss of ions traversing cold matter is the Bethe-Bloch formulation^{31–33} where the dominant loss mechanism is due to collisions with electrons in the material. For protons with $\gtrsim \text{MeV}$ energies, Geant4 uses a Bethe-Bloch model. However, ions traversing a plasma may also lose energy to the excitation of plasma waves, and at high enough temperatures and densities stopping by plasma ions (not electrons)

may dominate.³⁴ This contribution has been analytically formulated by Li and Petrasso³⁴ for plasmas with a Coulomb logarithm $\ln \Lambda \gtrsim 2$. The Bethe-Bloch model for ions in CM was compared with the Li-Petrasso stopping power in plasmas.

Contours of the plasma-to-CM stopping power ratio are shown in Figure 4(d) for 3 and 15 MeV protons in T - ρ space. At low temperature and low density, plasma stopping power strongly deviates from the CM value for these high energy protons. As temperature increases for a constant density, a temperature threshold is reached when the electron speed in the plasma is approximately the test proton speed, and the plasma stopping becomes weaker than that in cold matter of the same density. This threshold is clearly reached at a lower temperature for 3 MeV protons than 15 MeV protons, as expected. Plasma stopping is also weaker than CM at low temperatures and high densities because $\ln \Lambda$ decreases with increasing density. Again, to estimate the accuracy of the CM approximation, the sample trajectory is path-integrated on the surface in T - ρ space,

$$\Delta E \approx \int \left(\frac{dE}{dx} \right) dx. \quad (9)$$

It was found that 15 MeV protons would have $\sim 9\%$ higher stopping power in the plasma, whereas 3 MeV protons would have a lower stopping power by $\sim 8\%$. In these calculations, the absolute energy loss was assumed negligible and is sufficient for estimation purposes here.

The cold matter approximation has been shown to be accurate to $\lesssim 5\%$ for proton scattering and to $\lesssim 10\%$ for energy loss in the typical proton radiography experiments of laser-foil interactions. However, every experiment is different, and in some cases the CM approximation is insufficient and a more complicated plasma model will need to be used. Furthermore, the plasma stopping power model implemented here assumes a fully ionized plasma and represents an upper bound on the error of the CM approximation. Nevertheless, for experiments discussed here and in many laser-foil experiments, the CM approximation is adequate and within the uncertainty of the presented analytical models. For these reasons the collision physics currently implemented in Geant4 can be used to model trajectories in proton radiography experiments.

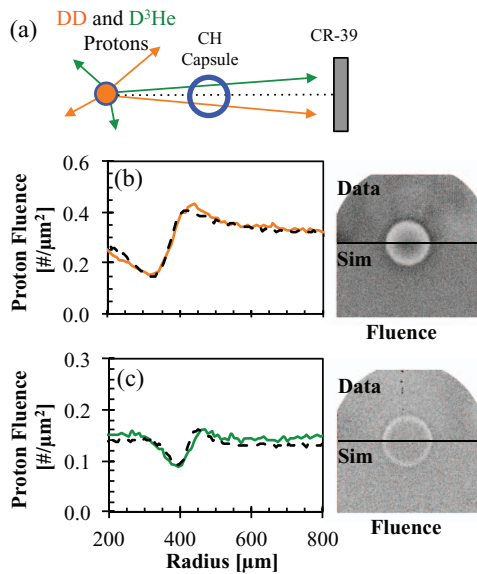


FIG. 5. (a) Experimental setup for capsule radiographs. Synthetic and experimental data are shown for 3 MeV (b) and 15 MeV (c) proton radiographs of an unimploded CH capsule from OMEGA shot 46531. The top half of either radiograph is from experimental data and the bottom half is simulated. Corresponding radial lineouts are shown by the solid line (experiment) and the dashed line (simulated).

B. Geant4 validation

Proton radiographs of non-irradiated targets were used to benchmark Geant4 simulations and validate the collision-physics package implementation. These “cold” targets were characterized and modeled in the Geant4 framework. Monoenergetic backlighter protons lost energy and were scattered in the targets due to Coulomb collisions. A 24 μm thick undriven CH shell was radiographed using 3 and 15 MeV protons. CR-39 detectors and the capsule target were aligned to be 25 cm and 1 cm, respectively, from the proton backlighter. The capsule target provided a useful benchmark for proton scattering through variable path lengths of material. Figures 5(b) and 5(c) show the comparison between synthetic and experimental radiographs for 3 and 15 MeV protons, respectively. Radial lineouts produced from synthetic Geant4 radiographs (dashed line) agreed very well with experimental data (solid line). In the D^3He proton fluence image, a $\sim 10\%$ discrepancy between simulation and experiment is observed

away from the capsule around $r \sim 800 \mu\text{m}$. However, the angular separation from the capsule shell to the edge of the plot is $\sim 2.3^\circ$, which is larger than the soft limit quoted in Sec. IV B of $\sim 1.1^\circ$. Therefore, a 10% discrepancy across $\sim 2.3^\circ$ may be tolerated. Experimental radiographs were aligned with synthetic radiographs for both energies and reproduced the observed data to within the accuracy of the experiment.

Proton fluence amplitude modulation was benchmarked using a variable frequency nickel mesh and CH foils of different thicknesses. The 35 μm thick nickel mesh was electroformed with hole spacings of $\lambda \sim 230, 150, 90 \mu\text{m}$; in this geometry, these spacings correspond to $f_\theta \sim 110, 170, 290 \text{ rad}^{-1}$, respectively. The mesh splits the quasi-isotropic proton flux into “beamlets” at variable spatial frequencies as schematically shown in Figure 6(a). The RMS amplitude modulation (α_{RMS}), using no additional CH, is shown to increase with hole spacing in Figure 6(b), as expected. A separate experiment had beamlets incident onto 25, 50, 75, and 100 μm thick CH foils. Lineouts taken of the resultant proton radiograph are shown in Figure 6(c) for the $\lambda \sim 230 \mu\text{m}$ wavelength. Proton fluence was normalized for the comparison of different CH thicknesses and amplitude modulation is shown to decrease with increased CH foil thickness as expected. The RMS amplitude modulation was calculated and plotted as a function of CH thickness for $\lambda \sim 230 \mu\text{m}$ (\circ) in Figure 6(d). Proton beamlets of $\lambda \sim 150 \mu\text{m}$ were only observed through the 25 μm thick foil, whereas $\lambda \sim 230 \mu\text{m}$ was measured through CH thicknesses up to 100 μm . However, beamlets of $\lambda \sim 90 \mu\text{m}$ were not resolvable through any of the CH thicknesses due to blurring caused by Coulomb scattering in the foil in addition to source size effects. Simulations of these experiments were found to track measured data reasonably well, thereby verifying the modeling capabilities for proton radiography in the Geant4 framework when the cold-matter approximation is sufficient to describe the Coulomb interactions.

Geant4 provides the user with the ability to simultaneously model particle interactions in a target and the subsequent detector physics in arbitrary geometries. This capability can be extremely useful for detectors with complex response functions, such as magnet-based spectrometers, detector systems which rely on nuclear reactions, or stacks of film. This capability has been exploited in Geant4 to determine the

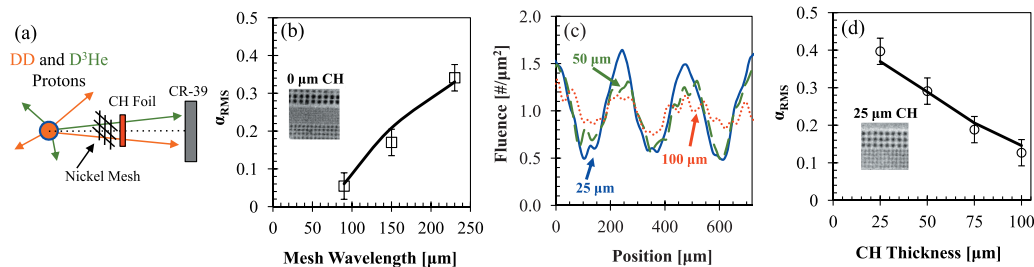


FIG. 6. (a) Experimental setup for mesh radiography experiments. (b) Measured RMS amplitude modulation (\square) through the nickel mesh only is plotted as a function of hole spacing with simulated results (solid line). The experimental radiograph shown is from OMEGA shot 44429 and illustrates the three different mesh frequencies. (c) Normalized proton fluence lineouts from data taken on OMEGA shot 44431. Amplitude modulation is shown to decrease for the $\lambda \sim 230 \mu\text{m}$ mesh as CH thickness is increased from 25 to 100 μm . (d) Measured RMS amplitude modulation (\circ) is plotted as a function of CH thickness with simulated results (solid line) for the $\lambda \sim 230 \mu\text{m}$ mesh hole spacing. The proton fluence radiograph of the mesh through 25 μm CH is shown with other mesh frequencies visible.

TABLE II. Comparison of proton source parameters for exploding-pusher and TNSA-generated MeV protons. Quantities given for the TNSA proton source are nominal and in many cases, as in pulse duration, peak energy, and source size, the values are dependent on the laser and target parameters. Additionally, CR-39 could be used as a detecting medium for TNSA-generated protons, though due to high fluences, saturation can be a problem.

	Exploding-pusher	TNSA
Source size [μm]	~ 45	~ 10
Duration (FWHM) [ps]	~ 150	$\sim 1-10$
Peak energy [MeV]	~ 15	~ 60
Energy spectrum	Monoenergetic	Exponential
Drive requirements	Multi-beam (implosion)	High-intensity ($\gtrsim 10^{19}$ W/cm 2)
Detecting medium	CR-39	RC Film
Detection process	proton counting (track detection)	dosimetric (optical depth)

response function³⁵ for magnet-based diagnostics, specifically the magnetic-recoil-spectrometer.^{36,37} Furthermore, the complex detector response of an exponential proton spectrum incident onto a filtered stack of radiochromic film, as in short-pulse proton radiography, may be self-consistently modeled in the Geant4 framework to deduce quantitative information from the images. In the work described here, monoenergetic 3 and 15 MeV protons were modeled through a target and then the detector stack for a comprehensive simulation of the experiment, from source to detector.

VI. SUMMARY

Monoenergetic proton radiography has been used in many experiments to measure path-integrated electromagnetic fields in high energy density plasmas where other methods prove ineffective. Proton emittance isotropy of these exploding-pusher backlighter capsules has been characterized on a global and local scale. Multiple yield diagnostics were fielded to quantify the global deviation of both proton species and were measured to be $\Sigma_{DD} \approx 16 \pm 7\%$ and $\Sigma_{D^3He} \approx 26 \pm 10\%$. Local variation was measured on single sheets of CR-39 using “blank” radiographs of the backlighter source. It was shown that local fluence variation was dominated by low angular frequency modes $f_\theta \lesssim 50 \text{ rad}^{-1}$ and that variations of a few percent should be expected on smaller spatial scales.

The exploding-pusher proton source discussed here has been recently used in many experiments and is in strong contrast to the TNSA-generated proton source used previously. A summary of characteristics for the two proton sources is given in Table II using typical parameters from OMEGA-EP (Ref. 38), though other facilities will have slightly different source characteristics. TNSA-generated protons typically have a smaller source size, shorter pulse duration, and higher peak energy than the exploding-pusher-generated protons. However, TNSA protons are produced in an exponential spectrum, where energy-loss in the target can create a degeneracy not present when using the monoenergetic source. The exploding-pusher source generates protons isotropically and can be utilized in multiple experiments in a single shot. Contrarily, the TNSA source protons are forwardly directed, but

can provide radiographs of the target at multiple times in a single shot due to the difference in proton time-of-flight.

Typical media for detecting protons also differ between the exploding-pusher and TNSA proton sources. The ability to count individual tracks and directly measure relative proton fluence using CR-39 removes the necessary deconvolution when using RC film. Using a mesh in an experiment, may remove the necessity of knowing the relative fluence to make a quantitative measurement at a cost of further energy degeneracy (in the case of TNSA) and at a cost to spatial resolution. These two complimentary diagnostic tools differ substantially in source characteristics and both come with a unique set of challenges. However, regardless of the proton source, Coulomb collisions in the target will cause energy-loss and scattering and these effects have been modeled and benchmarked for the monoenergetic, exploding-pusher source.

A new simulation tool has been developed to model monoenergetic proton radiography experiments using the Geant4 open-source framework. Realistic spectral source profiles, exact detector geometries, arbitrary electromagnetic field maps, and generic target mass distributions have been implemented. The physics packages currently used address Coulomb interactions in the cold-matter approximation and do not account for plasma effects. Due to the minimal amount of energy-loss and scattering experienced by MeV protons under plasma conditions discussed herein, the cold-matter approximation was shown to accurately approximate the collisional behavior to $\lesssim 10\%$, which is within the uncertainty of the analytic formulations used. Geant4 modeling was benchmarked against multiple experimental radiographs of non-irradiated targets. This simulation tool is used to generate synthetic radiographs for quantitative comparisons with experimental data as well as to aid in experimental design.

ACKNOWLEDGMENTS

The authors express their gratitude to the engineering staff at LLE for their support. The work described here was done as part of the first author’s Ph.D. dissertation and supported in part by NLUF (DE-NA0000877), FSC/UR (415023-G), DoE (DE-FG52-09NA29553), LLE (414090-G), and LLNL (B580243).

¹C. K. Li, F. H. Séguin, J. A. Frenje, J. R. Rygg, R. D. Petrasso, R. P. J. Town, P. A. Amendt, S. P. Hatchett, O. L. Landen, A. J. Mackinnon, P. K. Patel, V. A. Smalyuk, T. C. Sangster, and J. P. Knauer, *Phys. Rev. Lett.* **97**(13), 135003 (2006).

²C. K. Li, F. H. Séguin, J. A. Frenje, J. R. Rygg, R. D. Petrasso, R. P. J. Town, P. A. Amendt, S. P. Hatchett, O. L. Landen, A. J. Mackinnon, P. K. Patel, V. A. Smalyuk, J. P. Knauer, T. C. Sangster, and C. Stoeckl, *Rev. Sci. Instrum.* **77**, 10E725 (2006).

³J. R. Rygg, F. H. Séguin, C. K. Li, J. A. Frenje, M. J.-E. Manuel, R. D. Petrasso, R. Betti, J. A. Delettrez, O. V. Gotchev, J. P. Knauer, D. D. Meyerhofer, F. J. Marshall, C. Stoeckl, and W. Theobald, *Science* **319**(5867), 1223–1225 (2008).

⁴C. K. Li, F. H. Séguin, J. A. Frenje, M. Rosenberg, R. D. Petrasso, P. A. Amendt, J. A. Koch, O. L. Landen, H. S. Park, H. F. Robey, R. P. J. Town, A. Casner, F. Philippe, R. Betti, J. P. Knauer, D. D. Meyerhofer, C. A. Back, J. D. Kilkenny, and A. Nikroo, *Science* **327**(5970), 1231–1235 (2010).

⁵F. H. Séguin, C. K. Li, M. J.-E. Manuel, H. G. Rinderknecht, N. Sinenian, J. A. Frenje, J. R. Rygg, D. G. Hicks, R. D. Petrasso, J. Delettrez, R. Betti, F. J. Marshall, and V. A. Smalyuk, *Phys. Plasmas* **19**, 012701 (2012).

- ⁶F. H. Séguin, J. A. Frenje, C. K. Li, D. G. Hicks, S. Kurebayashi, J. R. Rygg, B. E. Schwartz, R. D. Petrasso, S. Roberts, J. M. Soures, D. D. Meyerhofer, T. C. Sangster, J. P. Knauer, C. Sorce, V. Yu Glebov, C. Stoeckl, T. W. Phillips, R. J. Leeper, K. Fletcher, and S. Padalino, *Rev. Sci. Instrum.* **74**(2), 975–995 (2003).
- ⁷M. J. E. Manuel, M. J. Rosenberg, N. Sinenian, H. Rinderknecht, A. B. Zylstra, F. H. Seguin, J. Frenje, C. K. Li, and R. D. Petrasso, *Rev. Sci. Instrum.* **82**(9), 095110–095110–8 (2011).
- ⁸N. Sinenian, M. Rosenberg, M. J. E. Manuel, S. C. McDuffee, F. H. Séguin, J. A. Frenje, C. K. Li, and R. D. Petrasso, *Rev. Sci. Instrum.* **82**(10), 7 (2011).
- ⁹A. B. Zylstra, H. G. Rinderknecht, N. Sinenian, M. J. Rosenberg, M. Manuel, F. H. Seguin, D. T. Casey, J. A. Frenje, C. K. Li, and R. D. Petrasso, *Rev. Sci. Instrum.* **82**(8), 083301–7 (2011).
- ¹⁰S. P. Hatchett, C. G. Brown, T. E. Cowan, E. A. Henry, J. S. Johnson, M. H. Key, J. A. Koch, A. B. Langdon, B. F. Lasinski, R. W. Lee, A. J. Mackinnon, D. M. Pennington, M. D. Perry, T. W. Phillips, M. Roth, T. C. Sangster, M. S. Singh, R. A. Snavely, M. A. Stoyer, S. C. Wilks, and K. Yasuike, *Phys. Plasmas* **7**(5), 2076–2082 (2000).
- ¹¹A. J. Mackinnon, P. K. Patel, R. P. Town, M. J. Edwards, T. Phillips, S. C. Lerner, D. W. Price, D. Hicks, M. H. Key, S. Hatchett, S. C. Wilks, M. Borghesi, L. Romagnani, S. Kar, T. Toncian, G. Pretzler, O. Willi, M. Koenig, E. Martinolli, S. Lepape, A. Benuzzi-Mounaix, P. Audebert, J. C. Gauthier, J. King, R. Snavely, R. R. Freeman, and T. Boehlly, *Rev. Sci. Instrum.* **75**(10), 3531–3536 (2004).
- ¹²A. B. Zylstra, C. K. Li, H. G. Rinderknecht, F. H. Séguin, R. D. Petrasso, C. Stoeckl, D. D. Meyerhofer, P. Nilson, T. C. Sangster, and S. Le Pape, *Rev. Sci. Instrum.* **83**(1), 013511–013511–9 (2012).
- ¹³R. A. Snavely, M. H. Key, S. P. Hatchett, T. E. Cowan, M. Roth, T. W. Phillips, M. A. Stoyer, E. A. Henry, T. C. Sangster, and M. S. Singh, *Phys. Rev. Lett.* **85**(14), 2945–2948 (2000).
- ¹⁴Nicholas Metropolis and S. Ulam, *J. Am. Stat. Assoc.* **44**(247), 335–341 (1949) (<http://www.jstor.org/stable/2280232>).
- ¹⁵S. Agostinelli, J. Allison, K. Amako, J. Apostolakis, H. Araujo, P. Arce, M. Asai, D. Axen, S. Banerjee, G. Barrand, F. Behner, L. Bellagamba, J. Boudreau, L. Broglia, A. Brunengo, H. Burkhardt, S. Chauvie, J. Chuma, R. Chytracsek, G. Cooperman, G. Cosmo, P. Degtyarenko, A. Dell'Acqua, G. Depaola, D. Dietrich, R. Enami, A. Feliciello, C. Ferguson, H. Fesefeldt, G. Folger, F. Foppiano, A. Forti, S. Garelli, S. Giani, R. Gianintrapani, D. Gibin, J. J. Gómez Cadenas, I. González, G. Gracia Abril, G. Greeniaus, W. Greiner, V. Grichine, A. Grossheim, S. Guatelli, P. Gumplinger, R. Hamatsu, K. Hashimoto, H. Hasui, A. Heikkinen, A. Howard, V. Ivanchenko, A. Johnson, F. W. Jones, J. Kallenbach, N. Kanaya, M. Kawabata, Y. Kawabata, M. Kawaguti, S. Kelner, P. Kent, A. Kimura, T. Kodama, R. Kokoulin, M. Kossov, H. Kurashige, E. Lamanna, T. Lampén, V. Lara, V. Lefebvre, F. Lei, M. Liendl, W. Lockman, F. Longo, S. Magni, M. Maire, E. Medernach, K. Minamimoto, P. Mora de Freitas, Y. Morita, K. Murakami, M. Nagamatu, R. Nartallo, P. Nieminen, T. Nishimura, K. Ohtsubo, M. Okamura, S. O'Neale, Y. Oohata, K. Paech, J. Perl, A. Pfeiffer, M. G. Pia, F. Ranjard, A. Rybin, S. Sadilov, E. Di Salvo, G. Santin, T. Sasaki, N. Savvas, Y. Sawada *et al.*, *Nucl. Instrum. Methods: Phys. Res. A* **506**(3), 250–303 (2003).
- ¹⁶J. Allison, K. Amako, J. Apostolakis, H. Araujo, P. Arce Dubois, M. Asai, G. Barrand, R. Capra, S. Chauvie, R. Chytracsek, G. A. P. Cirrone, G. Cooperman, G. Cosmo, G. Cuttone, G. G. Daquino, M. Donszelmann, M. Dressel, G. Folger, F. Foppiano, J. Generowicz, V. Grichine, S. Guatelli, P. Gumplinger, A. Heikkinen, I. Hrivnacova, A. Howard, S. Incerti, V. Ivanchenko, T. Johnson, F. Jones, T. Koi, R. Kokoulin, M. Kossov, H. Kurashige, V. Lara, S. Larsson, F. Lei, O. Link, F. Longo, M. Maire, A. Mantero, B. Mascialino, I. McLaren, P. Mendez Lorenzo, K. Minamimoto, K. Murakami, P. Nieminen, L. Pandola, S. Parlati, L. Peralta, J. Perl, A. Pfeiffer, M. G. Pia, A. Ribon, P. Rodrigues, G. Russo, S. Sadilov, G. Santin, T. Sasaki, D. Smith, N. Starkov, S. Tanaka, E. Tcherniaev, B. Tom, A. Trindade, P. Truscott, L. Urban, M. Verderi, A. Walkden, J. P. Wellisch, D. C. Williams, D. Wright, and H. Yoshida, *IEEE Trans. Nucl. Sci.* **53**(1), 270–278 (2006).
- ¹⁷T. R. Boehly, D. L. Brown, R. S. Craxton, R. L. Keck, J. P. Knauer, J. H. Kelly, T. J. Kessler, S. A. Kumpan, S. J. Loucks, S. A. Letzring, F. J. Marshall, R. L. McCrory, S. F. B. Morse, W. Seka, J. M. Soures, and C. P. Verdon, *Opt. Commun.* **133**(1–6), 495–506 (1997).
- ¹⁸Depending on the particular experimental configuration, more beams may be used to provide more laser energy on target.
- ¹⁹D. G. Hicks, C. K. Li, F. H. Séguin, J. D. Schnittman, A. K. Ram, J. A. Frenje, R. D. Petrasso, J. M. Soures, D. D. Meyerhofer, S. Roberts, C. Sorce, C. Stoeckl, T. C. Sangster, and T. W. Phillips, *Phys. Plasmas* **8**(2), 606–610 (2001).
- ²⁰J. A. Frenje, C. K. Li, F. H. Séguin, J. Deciantis, S. Kurebayashi, J. R. Rygg, R. D. Petrasso, J. Delettrez, V. Yu Glebov, C. Stoeckl, F. J. Marshall, D. D. Meyerhofer, T. C. Sangster, V. A. Smalyuk, and J. M. Soures, *Phys. Plasmas* **11**, 2798–2805 (2004).
- ²¹D. G. Hicks, C. K. Li, R. D. Petrasso, F. H. Séguin, B. E. Burke, J. P. Knauer, S. Cremer, R. L. Kremens, M. D. Cable, and T. W. Phillips, *Rev. Sci. Instrum.* **68**, 589–592 (1997).
- ²²D. G. Hicks, “Charged-Particle Spectroscopy: A New Window on Inertial Confinement Fusion,” Ph.D. dissertation (Massachusetts Institute of Technology, 1999).
- ²³F. H. Séguin, C. K. Li, J. A. Frenje, S. Kurebayashi, R. D. Petrasso, F. J. Marshall, D. D. Meyerhofer, J. M. Soures, T. C. Sangster, C. Stoeckl, J. A. Delettrez, P. B. Radha, V. A. Smalyuk, and S. Roberts, *Phys. Plasmas* **9**(8), 3558–3566 (2002).
- ²⁴William H. Press, Saul A. Teukolsky, William T. Vetterling, and Brian P. Flannery, *Numerical Recipes in C++: The Art of Scientific Computing Second Edition*, 2nd ed. (Cambridge University Press, 2002).
- ²⁵The QGSP BERT physics package was used.
- ²⁶John David Jackson, *Classical Electrodynamics*, 3rd ed. (Wiley, New York, 1999).
- ²⁷Jeffrey Freidberg, *Plasma Physics and Fusion Engineering* (Cambridge University Press, Cambridge, United Kingdom, 2007).
- ²⁸J. L. DeCiantis, F. H. Séguin, J. A. Frenje, V. Berube, M. J. Canavan, C. D. Chen, S. Kurebayashi, C. K. Li, J. R. Rygg, B. E. Schwartz, R. D. Petrasso, J. A. Delettrez, S. P. Regan, V. A. Smalyuk, J. P. Knauer, F. J. Marshall, D. D. Meyerhofer, S. Roberts, T. C. Sangster, C. Stoeckl, K. Mikaelian, H. S. Park, and H. F. Robey, *Rev. Sci. Instrum.* **77**(4), 043503–9 (2006).
- ²⁹D. Keller, T. J. B. Collins, J. A. Delettrez, P. W. McKenty, P. B. Radha, R. P. J. Town, B. Whitney, and G. A. Moses, “DRACO—A new multidimensional hydrocode,” November 15–19, 1999.
- ³⁰P. B. Radha, V. N. Goncharov, T. J. B. Collins, J. A. Delettrez, Y. Elbaz, V. Yu Glebov, R. L. Keck, D. E. Keller, J. P. Knauer, J. A. Marozas, F. J. Marshall, P. W. McKenty, D. D. Meyerhofer, S. P. Regan, T. C. Sangster, D. Shvarts, S. Skupsky, Y. Srebro, R. P. J. Town, and C. Stoeckl, *Phys. Plasmas* **12**(3), 032702–18 (2005).
- ³¹H. Bethe, *Ann. Phys.* **397**(3), 325–400 (1930).
- ³²F. Bloch, *Ann. Phys.* **408**(3), 285–320 (1933).
- ³³W. R. Leo, *Techniques for Nuclear and Particle Physics Experiments: A How-to Approach* (Springer, 1994).
- ³⁴Chi-Kang Li and Richard D. Petrasso, *Phys. Rev. Lett.* **70**(20), 3059 (1993).
- ³⁵D. T. Casey, “Diagnosing inertial confinement fusion implosions at OMEGA and the NIF using novel neutron spectrometry,” Ph.D. dissertation (Massachusetts Institute of Technology, 2011).
- ³⁶J. A. Frenje, D. T. Casey, C. K. Li, J. R. Rygg, F. H. Séguin, R. D. Petrasso, V. Yu Glebov, D. D. Meyerhofer, T. C. Sangster, S. Hatchett, S. Haan, C. Cerjan, O. Landen, M. Moran, P. Song, D. C. Wilson, and R. J. Leeper, *Rev. Sci. Instrum.* **79**(10), 10E502–6 (2008).
- ³⁷D. T. Casey, J. A. Frenje, M. Gatu Johnson, M. J. E. Manuel, H. G. Rinderknecht, N. Sinenian, F. H. Séguin, C. K. Li, R. D. Petrasso, P. B. Radha, J. A. Delettrez, V. Yu Glebov, D. D. Meyerhofer, T. C. Sangster, D. P. McNabb, P. A. Amendt, R. N. Boyd, J. R. Rygg, H. W. Herrmann, Y. H. Kim, and A. D. Bacher, *Phys. Rev. Lett.* **108**(7), 075002 (2012).
- ³⁸L. J. Waxer, D. N. Maywar, J. H. Kelly, T. J. Kessler, B. E. Kruschwitz, S. J. Loucks, R. L. McCrory, D. D. Meyerhofer, S. F. B. Morse, C. Stoeckl, and J. D. Zuegel, *Opt. Photonics News* **16**(7), 30–36 (2005).